Regular Article

Reinforced atomically dispersed Fe—N—C catalysts derived from petroleum asphalt for oxygen reduction reaction

Qingshan Zhao, Xiaojie Tan, Tianwen Ma, Fengliang Cao, Zhengzheng Xia, Hui Liu, Hui Ning, Zhongtao Li, Han Hu, Mingbo Wu *

College of Chemical Engineering, College of New Energy, Institute of New Energy, State Key Laboratory of Heavy Oil Processing, China University of Petroleum (East China), Qingdao 266580, People's Republic of China

GRAPHICAL ABSTRACT
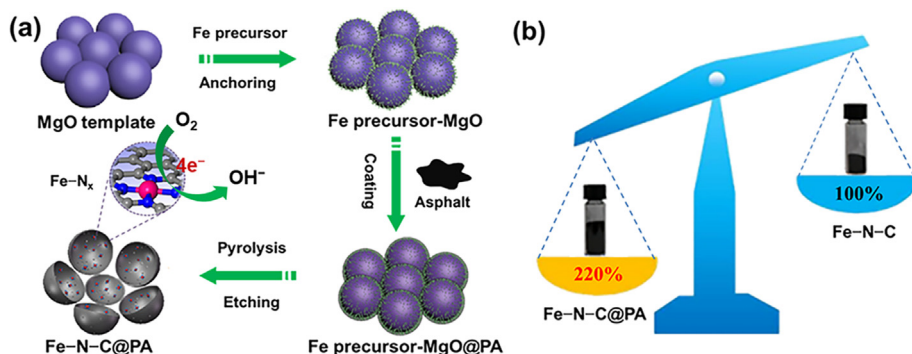
ARTICLE INFO

ABSTRACT

Massive production of efficient, durable, and low-cost electrocatalysts toward oxygen reduction reaction (ORR) is urgently desired for the development of energy storage and conversion devices. In this study, a facile and cost-effective strategy is proposed for the scalable synthesis of atomically dispersed Fe—N—C derived from petroleum asphalt (Fe—N—C@PA) as a reinforced catalyst for ORR. The Fe—N—C@PA is fabricated through a layer-by-layer cladding template and subsequent pyrolysis method. Intercalating appropriate amount of petroleum asphalt not only improves the graphitic degree to reinforce the atomic Fe—N_x active sites, but also increases mass yield of the catalyst (~220%) compared with the Fe—N—C counterpart. Serving as an ORR electrocatalyst, the optimized Fe—N—C@PA-1:4 provides almost a four-electron transfer pathway (3.96) and exhibits superior electrocatalytic activity with a half-wave potential ($E_{1/2}$) of 0.90 V to the commercial Pt/C catalyst ($E_{1/2}$ = 0.86 V), as well as promoted durability and methanol tolerance in alkaline medium. Moreover, the zinc-air battery based on Fe—N—C@PA-1:4 cathode delivers a high power density of 166.7 mW cm^{-2}. This work may help the massive production of robust atomically dispersed non-noble metal catalysts for ORR and provide a new avenue for the high value-added utilization of petroleum asphalt.

1. Introduction

The rapid economic development based on traditional fossil fuels has caused increasing concerns about environmental

* Corresponding author.
  E-mail addresses: qszhao@upc.edu.cn (Q. Zhao), wumb@upc.edu.cn (M. Wu).

pollution and energy crisis. Therefore, developing sustainable energy storage and conversion technologies is of great significance. Among the developed energy-related devices, fuel cells and rechargeable metal-air batteries show great potential owing to the high specific energy and environmental friendliness [1–4]. However, one of the main factors that hinders the commercialization and large-scale application is the sluggish kinetics of oxygen reduction reaction (ORR) occurring on their cathodes [5]. At present, Pt/C is commonly employed as the ORR catalyst, which still suffers from high price, scarce resource of platinum, and susceptibility to poisoning [6–8]. There is an urgent call for seeking high-performance, durable, and low-cost electrocatalysts for ORR.

In recent years, transition metal-nitrogen-carbon materials (M—N—C, M = Fe, Co, Ni etc.), especially Fe—N—C catalysts, have been triggered intensive attention as promising alternatives to Pt-based noble catalysts for ORR [9–14]. Among them, with isolated metal atoms stabilized on carbon matrices, atomically dispersed Fe—N—C catalysts not only maximize the utilization efficiency of metal atoms, but also modulate the electronic structures via electron interaction between the metal and support, leading to even superior catalytic performance to Pt/C catalyst [15–17]. For instance, Zhang et al. fabricated 2D porous carbon nanosheets with atomically-dispersed Fe—N_x—C active sites and large specific surface area based on regenerated silk fibroin. The Fe—N_x—C catalyst showed superior electrochemical activity toward ORR with a half-wave potential ($E_{1/2}$) of 0.853 V and remarkable stability with 11 mV loss in $E_{1/2}$ after 30,000 cycles [15]. Sun et al. developed an atomically dispersed Fe—N—C catalyst through a dual-MOFs (including ZIF-8 and MIL-101(Fe)) pyrolysis strategy, which exhibited a comparable ORR activity with the commercial Pt/C possessing a $E_{1/2}$ of 0.78 V in acids, as well as excellent methanol tolerance and stability [18]. Kuang et al. reported an ORR electrocatalyst with atomically dispersed Fe—N_4 sites anchored on 3D hierarchically ordered porous nitrogen-doped carbon by pyrolysis of ferrocene-encapsulated ZIF-8. The catalyst showed an outstanding ORR activity ($E_{1/2}$ = 0.875 V) and stability (changed 2 mV after 10,000 cycles) in alkaline medium, outperforming commercial Pt/C [19]. As to atomically dispersed Fe—N—C catalysts, the spatial confinement and electronic interaction induced by the substrates greatly affect the refined structure and catalytic property of Fe—N_x active sites [11]. Therefore, rational design of the carbonaceous substrates is crucial to further improve the electrocatalytic activity and stability. Moreover, complicated procedure or low yield of the catalysts may restrict the scalable synthesis and practical applications. Massive production of cost-effective but efficient atomically dispersed Fe—N—C catalysts is still urgently desired.

As a by-product of oil refining process, petroleum asphalt is generally utilized in basic paving and building industry due to its high viscosity and hydrophobic nature. In fact, petroleum asphalt is rich in large cyclic aromatic compounds, which can be readily crosslinked and carbonized under heat treatment, leading to porous carbon, carbon nanosheet, carbon fiber, and other functional carbon materials [20,21]. In particular, petroleum asphalt-based carbon materials with porous structure and high degree of graphitization serve as suitable substrates for catalytic active species [22–24]. Through rational design of the material structure, efficient ORR catalysts derived from petroleum asphalt with low cost and high yield can be developed [25].

Herein, a petroleum asphalt-derived atomically dispersed iron catalyst (Fe—N—C@PA) was fabricated for the first time and served as a reinforced catalyst for ORR. Iron precursor was firstly anchored on the surface of nano-MgO template, which was further coated with highly viscous petroleum asphalt. Such layer-by-layer cladding structure can suppress metal agglomeration in subsequent pyrolysis process, leading to the controllable synthesis of atomic Fe—N_x moieties. Intercalating appropriate amount of petroleum asphalt also significantly increases the graphitic degree and mass yield of the catalyst. The influence of coating amount of petroleum asphalt, metal precursor structure, and template type were systematically studied. Owing to the highly active and strengthened Fe—N_x species, the optimized Fe—N—C@PA-1:4 exhibits superior electrocatalytic activity, promoted durability, and excellent methanol tolerance for ORR under alkaline condition. The Fe—N—C@PA-1:4 catalyst also presents excellent performance when utilized as the cathode for zinc-air battery.

2. Experimental

2.1. Chemicals

Petroleum asphalt was obtained from China National Petroleum Corporation. MgO nanoparticles (50 nm), ZnO nanoparticles (50 nm), TiO$_2$ nanoparticles (50 nm), SiO$_2$ nanoparticles (50 nm), HCl (36–38 wt%) KOH (99 wt%) and KSCN (99 wt%) were purchased from Sinopharm Chemical Reagent Co., Ltd. Toluene (99 wt%), ferrous acetate (99 wt%), 1,10-phenanthroline (99 wt%), 2,2′-dipyridyl (99 wt%), 1,2-diaminobenzene (99 wt%), phthalocyanine (99 wt%) and methanol (90 wt%) were purchased from Aladdin Industrial Corporation. All reagents were used as received without further purification.

2.2. Synthesis

Initially, 0.106 g Fe(OAc)$_2$ and 0.330 g 1,10-phenanthroline were dissolved in ethanol and stirred for 2 h. Then, 3.16 g nano-MgO template was added into the solution and mixed evenly with ultrasound for 30 min to anchor the iron precursor. The mixed solution was heated at 60 °C to remove the solvent, followed by mixing into a toluene solution containing 0.79 g of petroleum asphalt. After intensive stirring, the colloid was dried at 70 °C and carbonized at 800 °C under nitrogen atmosphere for 2 h with a heating rate of 2 °C min^{-1}. The powder was immersed into 1 M HCl solution and stirred for 6 h to remove the residual template. The obtained Fe—N—C@PA-1:4 was washed with water until neutral and dried under vacuum at 60 °C. According to the mass ratio of petroleum asphalt/template, Fe—N—C@PA-1:3 and Fe—N—C@PA-1:5 catalysts were prepared. For comparison, Fe—N—C was prepared through the same procedure except for the addition of petroleum asphalt. Fe—N—C/NT was prepared in the absence of template and petroleum asphalt. MgO, ZnO, TiO$_2$, and SiO$_2$ nanoparticles with the same size were utilized as the template to obtain Fe—N—C@PA-MgO, Fe—N—C@PA-ZnO, Fe—N—C@PA-TiO$_2$ and Fe—N—C@PA-SiO$_2$, respectively. To investigate the influence of metal precursor structure, nitrogen-containing organics including 1,10-phenanthroline (L1), 2,2′-dipyridyl (L2), 1,2-diaminobenzene (L3), and phthalocyanine (L4) were employed as the ligand to obtain Fe—N—C@PA-L1, Fe—N—C@PA-L2, Fe—N—C@PA-L3, and Fe—N—C@PA-L4, respectively.

2.3. Characterization

Scanning electron microscopy (SEM) images were recorded on a Hitachi S-4800 instrument. Transmission electron microscopy (TEM) images and energy dispersive X-Ray spectroscopy (EDX) were recorded on a JEM-2100 microscope operating at 200 kV. High-angle annular dark-field scanning transmission electron microscopy (HAADF-STEM) images were carried out on a spherical aberration corrected Titan 80-300 operated at 300 kV. The nitrogen adsorption–desorption isotherm measurement was obtained at 77 K on a sorptometer (Micromeritics, ASAP 2020). Raman analysis was tested on an Advantage 785TM Raman spectrometer. X-ray

Q. Zhao, X. Tan, T. Ma et al.

photoelectron spectroscopy (XPS) analysis was conducted on a Kratos Axis Ultra instrument. The metal loading was measured on by inductively coupled plasma-atomic emission spectroscopy (ICP-AES, AGILENT730ES). X-ray absorption near edge structure (XANES) and extend X-ray absorption fine structure (EXAFS) were performed at 1W1B station in Beijing Synchrotron Radiation Facility (BSRF). Electrochemical impedance spectroscopy (EIS) tests were conducted on a CHI760E electrochemistry workstation at a frequency range of 100 KHz to 10 MHz with an AC voltage amplitude of 5 mV.

2.4. Electrochemical measurements

Electrochemical measurements were performed on a CHI760E electrochemical workstation with a standard three-electrode cell system. A rotating ring-disk electrode (RRDE) with a glassy carbon disk (GCE, 4 mm in diameter) was loaded with the as-prepared catalysts, serving as the working electrode. Ag/AgCl (saturated KCl) electrode and Pt wire were used as the reference electrode and counter electrode, respectively. Specifically, 2 mg catalyst was dispersed in 0.8 mL of ethanol and 5 μL of Nafion solution (5 wt%) to get a homogeneous catalyst ink, 15 μL of which was loaded onto the GCE and dried in air. As a control, commercial Pt/C (20 wt%) was prepared by the similar method with the same catalyst loading of 0.30 mg cm^{-2}. The potentials are referred to a reversible hydrogen electrode ($E_{RHE} = E_{Ag/AgCl} + 0.0591$ pH + 0.197 V). Cyclic voltammetry (CV) tests were conducted in an O_2 saturated 0.1 M KOH at a scan rate of 0.1 V s^{-1}. Linear-sweep voltammetry (LSV) measurements were performed at a scan rate of 5 mV s^{-1} under an electrode rotation rate of 1600 rpm. The poisoning experiment was performed by the addition of 5 mM KSCN into the electrolyte. Stability tests were conducted by the chronoamperometry measurements at the potential of 0.45 V for prolonged 200,000 s. For the methanol tolerance tests, 47.5 μL methanol was dissolved in 1 mL of 0.1 M KOH and added to the electrolyte at 300 s, and the current was collected at 0.565 V vs. RHE.

The peroxide percentage (H_2O_2%) and the electron transfer number (n) are determined by the following equations:

$$H_2O_2\% = 200 \times (I_R/N)/(I_D + I_R/N) \tag{1-1}$$

$$n = 4 \times I_D/(I_D + I_R/N) \tag{1-2}$$

where I_D is the disk current, I_R is the ring current, and N is current collection efficiency of the Pt ring. N is determined to be 0.40.

2.5. Zinc-air battery tests

Liquid zinc-air batteries were assembled to test the practical application of the catalysts. A zinc foil was used as the anode, and a carbon cloth (2 cm × 2 cm) loaded with catalyst loading amount of 1.0 mg cm^{-2} was employed as the air cathode, with 6 M KOH solution containing 0.2 M zinc acetate as the electrolyte. All the measurements were carried out with a CHI760E electrochemical workstation.

3. Results and discussion

The Fe—N—C@PA catalyst was facilely synthesized through a layer-by-layer cladding template and subsequent pyrolysis strategy, as shown in Fig. 1. Specifically, the iron precursor [Fe(phen)$_x$, phen = 1,10-phenanthroline] was firstly anchored and distributed on the surface of nano-MgO template, which was further coated with a thin layer of highly viscous petroleum asphalt. The layer-by-layer cladding structure can efficiently suppress metal migration and agglomeration in subsequent pyrolysis process, leading
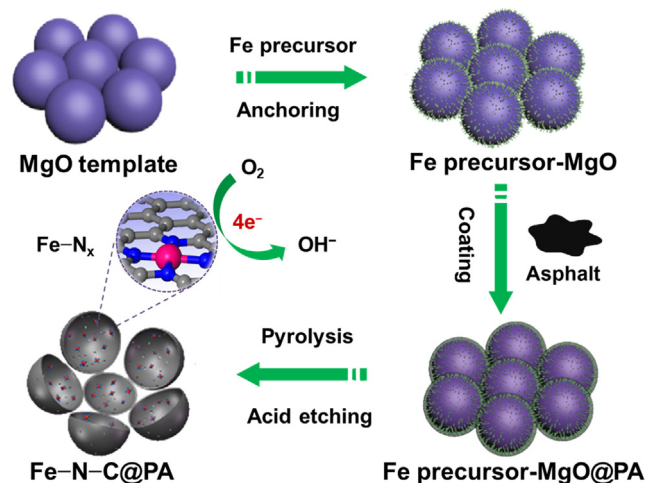

Fig. 1. Schematic illustration for the preparation procedure of Fe—N—C@PA.

to the controllable synthesis of atomic Fe—N$_x$ moieties. After acid etching of the spherical template, atomically dispersed Fe—N—C@PA catalyst for four-electron ORR with a hollow nanoshell structure was readily fabricated. As a control, the Fe—N—C counterpart was also prepared with the same procedure expect for the addition of petroleum asphalt.

The morphology of Fe—N—C and Fe—N—C@PA-1:4 was firstly observed by scanning electron microscopy (SEM) and transmission electron microscopy (TEM) images. SEM images of Fe—N—C and Fe—N—C@PA-1:4 both exhibit a honeycomb nanoarchitecture consisted of abundant pores with a diameter around 50 nm, in accordance with the size of the nano-MgO template (Fig. S1). The TEM images further exhibit the porous characteristic of Fe—N—C and Fe—N—C@PA-1:4 with curved graphene walls (Fig. 2a, b). Magnified TEM images disclose the absence of visible particles in the samples, as can be seen from the insets of Fig. 2a, b. Thus, the metal distribution was further monitored by high-angle annular dark-field scanning transmission electron microscopy (HAADF-STEM). As shown in Fig. 2c, isolated Fe atoms are clearly identified by the bright dots marked with pink circles in the Fe—N—C sample. Interestingly, Fe—N—C@PA-1:4 also displays the existence of single Fe atoms (marked with yellow circles) with a higher loading density (Fig. 2d). This is confirmed by the fact that the iron loadings in Fe—N—C and Fe—N—C@PA-1:4 are determined to be 1.05 wt% and 2.49 wt% respectively according to inductively coupled plasma-atomic emission spectroscopy (ICP-AES) measurements (Table S1). The results illustrate that coating of petroleum asphalt can facilitate the formation of more atomically dispersed Fe sites on the carbon matrix. Moreover, without employing any template, Fe—N—C/NT shows a bulk structure with numerous agglomerated particles encapsulated in carbonaceous matrix (Fig. S2). The agglomerated particles should be iron oxide species generated in the pyrolysis process, which cannot be removed through acid etching due to the intimate coating of carbon layer on the surface, resulting in absolute shielding of the iron active species. The porous structure of Fe—N—C and Fe—N—C@PA-1:4 is further investigated by nitrogen adsorption/desorption analysis, which exhibits type IV isotherms with hysteresis loops (Fig. S3a). Fe—N—C@PA-1:4 shows a high BET surface area of 404.5 m^2 g^{-1}, which is smaller than that of Fe—N—C (606.3 m^2 g^{-1}). Corresponding pore distribution results reveal the existence of micropores, mesopores, and macropores in the two samples (Fig. S3b). Whereas the introduction of petroleum asphalt would block part of the micropores and result in the formation of more macropores, accounting for the reduced surface area of Fe—N—C@PA-1:4. Therefore, the
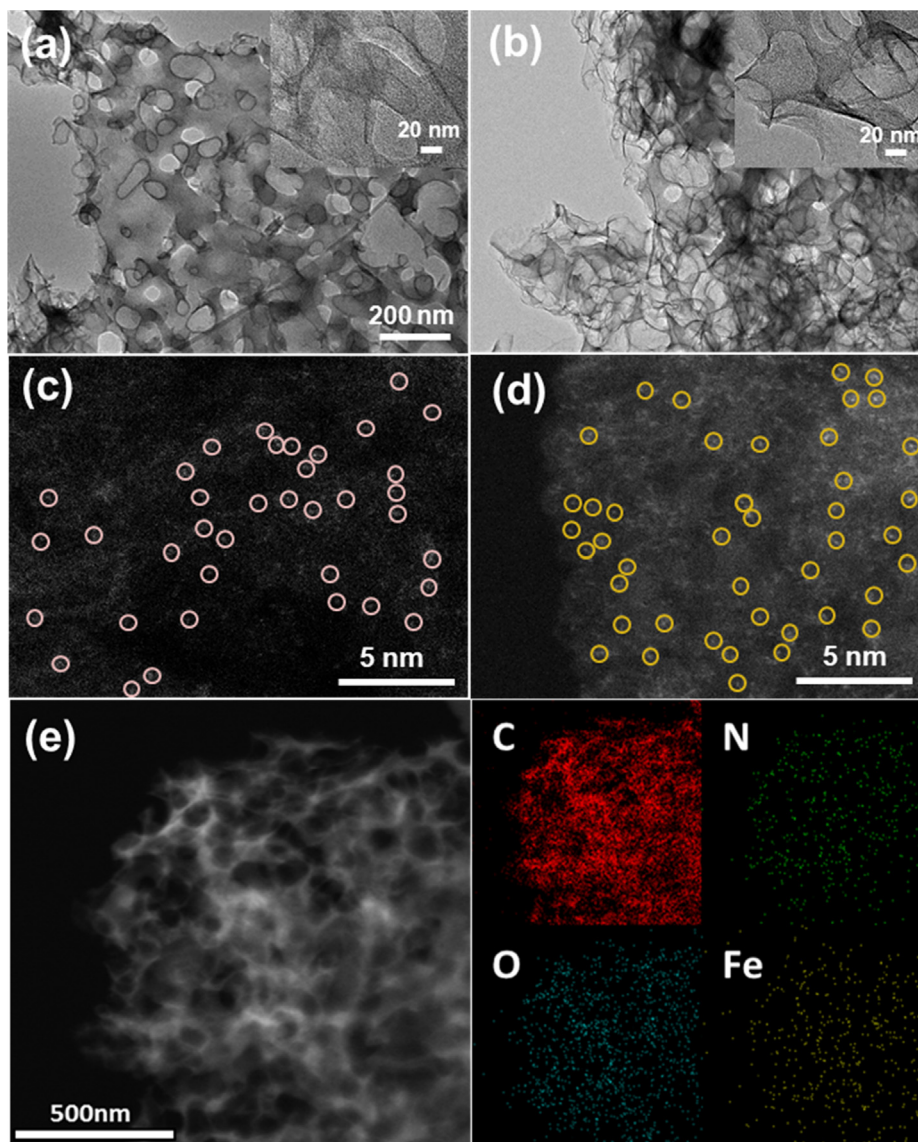
Fig. 2. TEM images of Fe—N—C (a) and Fe—N—C@PA-1:4 (b). HAADF-STEM images of Fe—N—C (c) and Fe—N—C@PA-1:4 (d). TEM image and corresponding EDX elemental mapping of Fe—N—C@PA-1:4 with C, N, O, and Fe elements (e).

nano-MgO template mainly provides a pore-forming effect and results in hierarchical pore structure of Fe—N—C and Fe—N—C@PA-1:4, which not only leads to the well exposure of the iron-based active sites, but also facilitates the transportation of O_2 and electrolyte during the electrocatalytic ORR process [26–27]. Fig. 2e shows a homogeneous distribution of C, N, O, and Fe elements on the carbon skeleton of Fe—N—C@PA-1:4. Since the above results have excluded the presence of iron oxide species, the O element should be mainly originated from oxygen doping to the carbon matrix.

X-ray photoelectron spectroscopy (XPS) analysis was conducted to study the surface composition and chemical valence state of the samples. Full range XPS spectra show the appearance of C, N, O, and Fe signals both in Fe—N—C and Fe—N—C@PA-1:4 (Fig. 3a). The Fe signal in Fe—N—C is not that clear probably due to its low content. High-resolution C 1s XPS spectrum of Fe—N—C@PA-1:4 shows a major sp^2 C=C peak centered at 284.3 eV, with three other peaks at 285.6, 286.2 and 288.4 eV corresponding to the binding energy of C—N, C—O and O—C=O, respectively (Fig. 3b) [28]. The functionalized oxygen-containing groups (C—O and O—C=O) on

the carbon matrix, which is further supported by the O1s XPS spectrum result (Fig. S4), can accelerate the contact between the electrolyte and electrode and facilitate mass transfer to the active sites. While the existence of C—N affords abundant coordination sites for Fe ions. This is confirmed by the N 1s XPS spectrum, which shows four peaks at 398.1, 400.3, 401.0 and 404.0 eV correspond to pyridinic N, pyrrolic N, graphitic N and oxidized N, respectively (Fig. 3c) [29]. The Fe—N peak located at 399.1 eV verifies the formation of Fe—N_x active species [12]. As shown in Fig. 3d, the Fe 2p spectrum can be deconvoluted into spin–orbit doublets of Fe^{3+} $2p_{1/2}$ at 725.5 eV and Fe^{3+} $2p_{3/2}$ at 713.1 eV, as well as Fe $2p_{1/2}$ (723.2 eV) and Fe $2p_{3/2}$ (709.7 eV) peaks of Fe^{2+}, with additional satellite peaks of Fe observed at 717.4 and 732.1 eV [30]. Accordingly, Fe^{2+} and Fe^{3+} species both exist in the Fe—N—C@PA-1:4 sample. Table S2 lists the elementary composition of Fe—N—C and Fe—N—C@PA-1:4. By contrast, Fe—N—C@PA-1:4 shows obviously higher contents of N (3.52 atomic%) and Fe (0.48 atomic %) than those of Fe—N—C (2.36 atomic% and 0.39 atomic%, respectively), suggesting the more Fe—N_x species in Fe—N—C@PA-1:4, in line with the above ICP-AES result. This phenomenon should
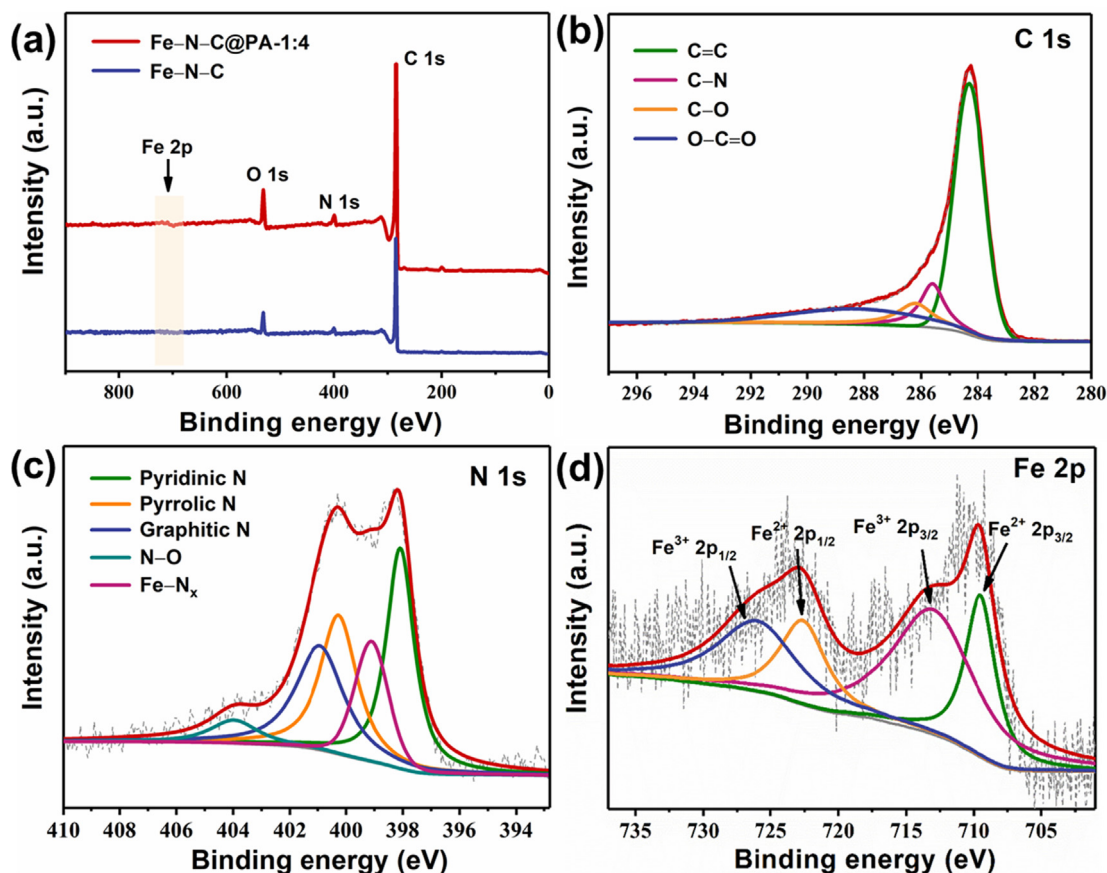
Fig. 3. Full range XPS spectra of Fe—N—C and Fe—N—C@PA-1:4 (a). High-resolution C 1s (b), N 1s (c) and Fe 2p (d) XPS spectrum of Fe—N—C@PA-1:4.

be resulted from the layer-by-layer cladding strategy, during which the highly viscous petroleum asphalt can prevent the decomposition of nitrogen-containing ligands and agglomeration of metal ions in the pyrolysis process, leading to the controllable formation of atomically dispersed Fe—N_x moieties [31].

To validate the single atom nature of the Fe—N_x active sites in Fe—N—C@PA-1:4, X-ray absorption spectroscopy (XAS) including X-ray absorption near edge structure (XANES) and extended X-ray absorption fine structure (EXAFS) spectra were further conducted. Fig. 4a shows the XANES curve of Fe—N—C@PA-1:4, along with the Fe foil, Fe_3O_4 and Fe_2O_3 references. From the inset of Fig. 4a, the magnified image reveals the absorption edge of

Fe—N—C@PA-1:4 is much higher than that of Fe foil and located between Fe_3O_4 and Fe_2O_3. Therefore, the average oxidation state of Fe in Fe—N—C@PA-1:4 is between 2+ and 3+, in well accordance with the XPS results [32]. A further compassion of the Fourier-transform k^3-weighted EXAFS curves reveals the presence of a primary peak located at 1.63 Å for Fe—N—C@PA-1:4, corresponding to the Fe—N coordination (Fig. 4b) [33]. The Fe—O peak at 1.48 Å and Fe—Fe peak at 2.23 Å are neglectable, suggesting the absence of FeO_x or metallic Fe in Fe—N—C@PA-1:4 [34]. The above results reveal that Fe coordinated with N to achieve atomic level Fe—N_x species have been successfully obtained as catalytic active sites for ORR.
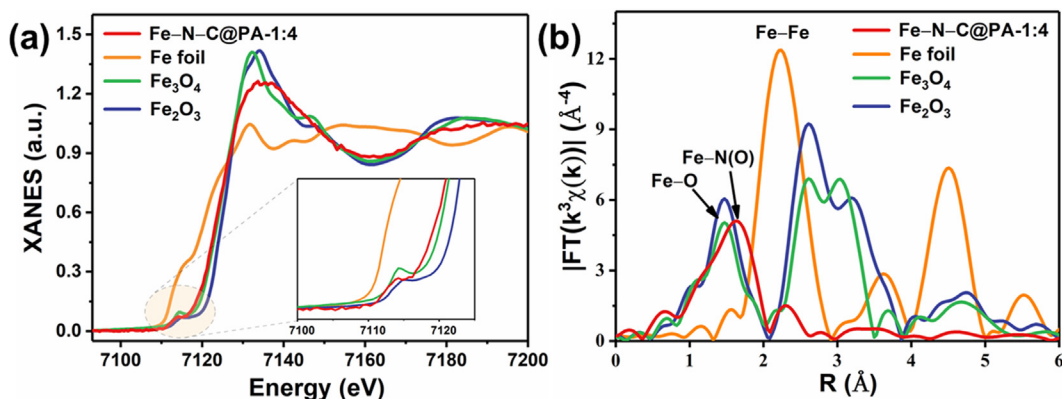

Fig. 4. XANES spectra at the Fe K-edge of Fe—N—C@PA-1:4, Fe foil, Fe_3O_4 and Fe_2O_3, and the inset is magnified image of the pre-edge XANES spectra (a). Fourier-transform EXAFS spectra of Fe—N—C@PA-1:4, Fe foil, Fe_3O_4 and Fe_2O_3 (b).

In order to explore the influence of petroleum asphalt on the material structure, Raman tests of Fe—N—C and Fe—N—C@PA-1:4 were further performed (Fig. 5a). The Raman spectra illustrate the presence of the D band at 1340 cm^{-1} associated with structure defects and disordering of carbon, as well as the G band at 1590 cm^{-1} corresponding to stretching vibration mode of graphite crystals [35]. Both Fe—N—C and Fe—N—C@PA-1:4 show $I_D{:}I_G$ values of around 1.0, reflecting relatively high graphitic degree of the samples, which might be ascribed to the catalytic graphitization effect of the nano-MgO template. A further study reveals the $I_D{:}I_G$ value of Fe—N—C@PA-1:4 decreases from 1.02 to 0.98, suggesting the even less disorder/defects with the addition of petroleum asphalt [36]. Moreover, the broad 2D region ranging from 2500 to 3100 cm^{-1} is mainly consisted of two distinguishable peaks at 2700 and 2860 cm^{-1}, which is similar to that of graphite or graphene oxide with multi defects [37]. The more prominent peak of Fe—N—C@PA-1:4 demonstrates higher graphitic degree of the carbon skeleton resulted from the petroleum asphalt-derived carbon layer, which would provide a conjugated electronic substrate for the trapping of atomic Fe—N_x sites. Remarkably, as shown in Fig. 5b, the obtained Fe—N—C@PA-1:4 achieves a dramatically enhanced mass yield of ~20% compared with the Fe—N—C counterpart. Therefore, the intercalation of petroleum asphalt not only facilitates the formation of atomically dispersed Fe—N_x sites on the carbonaceous substrate with high graphitic degree, but also provides a feasible and cost-effective avenue for the scalable synthesis (gram-scale and beyond, shown in Fig. S5) of non-noble metal catalysts for ORR.

The ORR electrocatalytic behaviors of the samples were firstly evaluated using cyclic voltammetry (CV) tests on a rotating ring-disk electrode (RRDE) in 0.1 M KOH solution (Fig. S6). Under O_2-saturated conditions, Fe—N—C and Fe—N—C@PA-1:4 exhibit obvious cathodic ORR peaks at 0.76 and 0.74 V (vs. RHE), respectively, suggesting effective oxygen reduction processes [38]. The more positive peak of Fe—N—C manifests its relatively higher catalytic activity than Fe—N—C@PA-1:4. Linear sweep voltammetry (LSV) measurements of the samples were further conducted. As seen in Fig. 6a, both Fe—N—C and Fe—N—C@PA-1:4 show comparable onset potentials (E_{onset}) to that of commercial Pt/C (~1.05 V) catalyst. Especially, the half-wave potential ($E_{1/2}$) of Fe—N—C@PA-1:4 is measured to be 0.90 V, which is nearly comparable to Fe—N—C (0.91 V) and 40 mV higher than that of Pt/C (0.86 V), indicating superior electrocatalytic ORR activity [39]. Moreover, Fe—N—C and Fe—N—C@PA-1:4 also afford higher limiting current densities than Pt/C due to their abundant porous structure. As a control, Fe—N—C/NT shows a poor ORR activity due to its bulk structure with absolute shielding of the iron active species. To evaluate the

influence of coating amount of petroleum asphalt, Fe—N—C@PA-1:3 and Fe—N—C@PA-1:5 were also prepared and tested. As can be seen, Fe—N—C@PA-1:3 shows much inferior E_{onset} and $E_{1/2}$ than that of Fe—N—C@PA-1:4, which should be attributed to partial shielding of the catalytic active sites induced by the excess of petroleum asphalt. Whereas insufficient petroleum asphalt would also cause incomplete surface coating of the template, leading to a reduced activity for Fe—N—C@PA-1:5. These results demonstrate the significant influence of coating amount of petroleum asphalt on the ORR performance, among which Fe—N—C@PA-1:4 stands out. As shown in Fig. 6b, the average electron transfer number (n) of Fe—N—C@PA-1:4 is calculated to be 3.96, with an ultralow H_2O_2 yield below 0.5% in the potential window from 0.2 to 0.6 V. While the average n of Fe—N—C@PA is only 3.76, and the yield of H_2O_2 is kept in the range of 0.8% to 1.5%. Therefore, in spite of showing a slightly lower $E_{1/2}$ than Fe—N—C, Fe—N—C@PA-1:4 exhibits a promoted four-electron transfer pathway for selective reduction of O_2 to OH^- rather than H_2O_2, which is of great significance for the application in fuel cell and metal-air battery devices [40].

As previously reported, the metal precursor structure may affect the fine structure of resulting Fe—N_x and makes an impact on the ORR performance [41]. Thus, Fe—N—C@PA samples were synthesized by employing various precursors with different nitrogen-containing ligands to coordinate with Fe ions, as illustrated in Fig. S7. According to the E_{onset} and $E_{1/2}$, the Fe—N—C@PA samples show good to excellent ORR catalytic activities compared with Pt/C (Fig. 6c). Among them, 1,10-phenanthroline serves as a dominant ligand to construct a stable coordination structure, facilitating the generation of favorable atomically dispersed Fe—N_x species. Moreover, to further evaluate the influence of template on the catalytic performance, MgO, ZnO, TiO_2, and SiO_2 nanoparticles with the same size were utilized as the template to obtain Fe—N—C@PA-MgO, Fe—N—C@PA-ZnO, Fe—N—C@PA-TiO_2, and Fe—N—C@PA-SiO_2, respectively. As shown in Fig. 6d, Fe—N—C@PA-MgO presents the maximum E_{onset} and $E_{1/2}$ values among the catalysts. Fe—N—C@PA-ZnO shows similar E_{onset} and $E_{1/2}$ to that of Fe—N—C@PA-MgO and presents a much higher limiting current density, which must be assigned to the multi micropores induced by zinc under high temperature, promoting internal mass diffusion in the ORR process [42]. In contrast, Fe—N—C@PA-SiO_2 and Fe—N—C@PA-TiO_2 show inferior catalytic activities towards ORR, which should be attributed to the weaker interaction of SiO_2 and TiO_2 with the metal precursor, resulting in tendentious formation of metal aggregations in the pyrolysis process [43]. Hence, besides the basic pore-forming effect, the template plays a crucial role on the active structure and catalytic performance [31]. Thereinto, MgO is
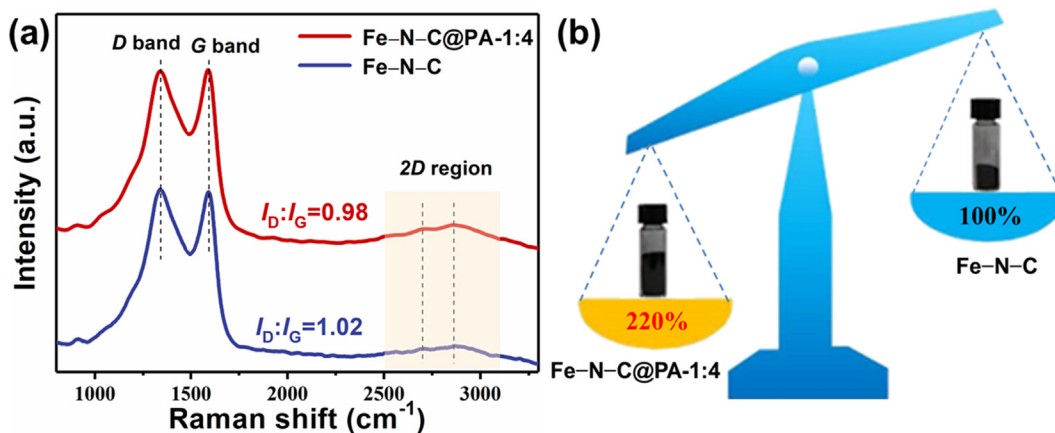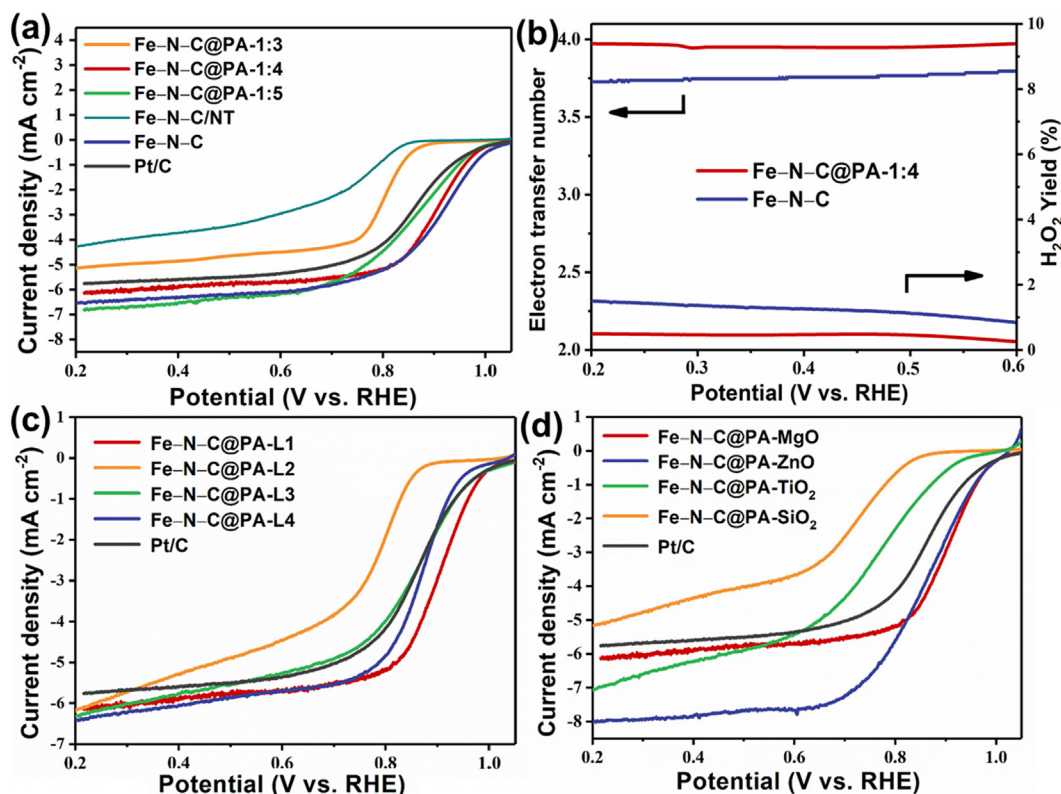
Fig. 5. Raman spectra of Fe—N—C and Fe—N—C@PA-1:4 (a). Comparison of the mass yield of Fe—N—C and Fe—N—C@PA-1:4 (b).

Fig. 6. LSV curves of Fe—N—C@PA with different coating amount of petroleum asphalt, Fe—N—C/NT, Fe—N—C, and Pt/C in O_2-saturated 0.1 M KOH solution (a). Electron transfer number and H_2O_2 yield at various potentials of Fe—N—C@PA-1:4 and Fe—N—C (b). LSV curves of Fe—N—C@PA prepared with different organic ligands and Pt/C (c). LSV curves of Fe—N—C@PA prepared with different templates and Pt/C (d).

determined to be a prominent template for the synthesis of efficient catalysts towards ORR.

Long-term stability of the catalyst is one of the most important parameters for ORR applications. The stability for Fe—N—C@PA-1:4, Fe—N—C and Pt/C catalysts were evaluated by the chronoamperometry measurements at the potential of 0.45 V. As shown in Fig. 7a, Fe—N—C and Pt/C catalysts present a rapid fading of the current density within 50,000 s, resulting in a retention rate of 88% and 72%, respectively. By contrast, Fe—N—C@PA-1:4 displays remarkable stability and delivers a 92% current retention rate with prolonged 200,000 s. That is to say, with the coating of petroleum asphalt-derived carbon layer, the active sites of Fe—N—C@PA-1:4 is reinforced and displays a promoted durability than Fe—N—C and Pt/C. Additionally, as anti-methanol interference ability is another important parameter for cathode catalysts in methanol fuel cells, the methanol tolerance tests of Fe—N—C@PA-1:4, Fe—N—C and Pt/C were conducted (Fig. 7b). When methanol is added into the electrolyte at 300 s, the current density of Pt/C shows an obvious disturbance, and a slight decrease can be observed for Fe—N—C. Whereas no visible change occurs for Fe—N—C@PA-1:4, unraveling its promoted methanol tolerance property.

In order to gain insights into the reaction mechanism, poisoning experiment was carried out to understand the intrinsic activity of Fe—N—C@PA-1:4. Compared with the catalytic performance of Fe—N—C@PA-1:4, a sharply declined activation area is shown in the CV curve after the addition of KSCN (Fig. S8). The LSV result further reveals the severely fading of E_{onset} and $E_{1/2}$ with the presence of SCN^- (Fig. 7c). This result demonstrates that the monodispersed Fe—N_x species are the dominant active centers for the efficient electrocatalytic oxygen reduction [44]. Electrochemical impedance spectroscopy (EIS) measurements were also employed to evaluate the kinetics of ORR over the catalysts. As shown in

Fig. 7d, Fe—N—C@PA-1:4 shows a much smaller diameter of semicircle in the high-frequency region than Fe—N—C, indicating the reduced interfacial charge transfer resistance [45]. This should be assigned to the higher graphitic degree and enhanced conductivity arising from the introduction of petroleum asphalt. Additionally, the slope of Fe—N—C@PA-1:4 is much higher than that of Fe—N—C in the low frequency region, which reflects that it's more convenient for ion diffusion across the catalyst [46]. Therefore, the versatile nanostructure and reinforced Fe—N_x species endow Fe—N—C@PA-1:4 as a remarkable catalyst for ORR.

Considering the superior ORR catalytic performance, liquid zinc-air batteries were further assembled by employing carbon cloth loaded with the catalysts as the air cathode and zinc foil as the anode. As shown in Fig. 8a, the zinc-air batteries based on Fe—N—C@PA-1:4 and Fe—N—C cathodes show ultrastable open-circuit voltages of 1.442 V and 1.414 V within 50,000 s, respectively. The Fe—N—C@PA-1:4 based battery achieves a high maximum power density of 166.7 mW cm^{-2}, which is also much larger than that of Fe—N—C (123.5 mW cm^{-2}), as shown in Fig. 8b. Additionally, the Fe—N—C@PA-1:4-based zinc-air battery delivers a stable charge and discharge potentials in a long term test of 100 h at a current density of 10 mA cm^{-2} (Fig. 8c). These results further reveal the significant role of petroleum asphalt and the reinforced ORR performance of Fe—N—C@PA-1:4 compared with the Fe—N—C counterpart. Additionally, Table S3 presents the performance comparison of Fe—N—C@PA-1:4 with recent reported Fe—N—C materials. Compared with the reported catalysts, Fe—N—C@PA-1:4 exhibits prominent electrocatalytic activity for ORR and provides an outstanding power density when utilized as the air cathode for a zinc-air battery, demonstrating great potential for the practical application of Fe—N—C@PA-1:4 in energy storage and conversion devices.
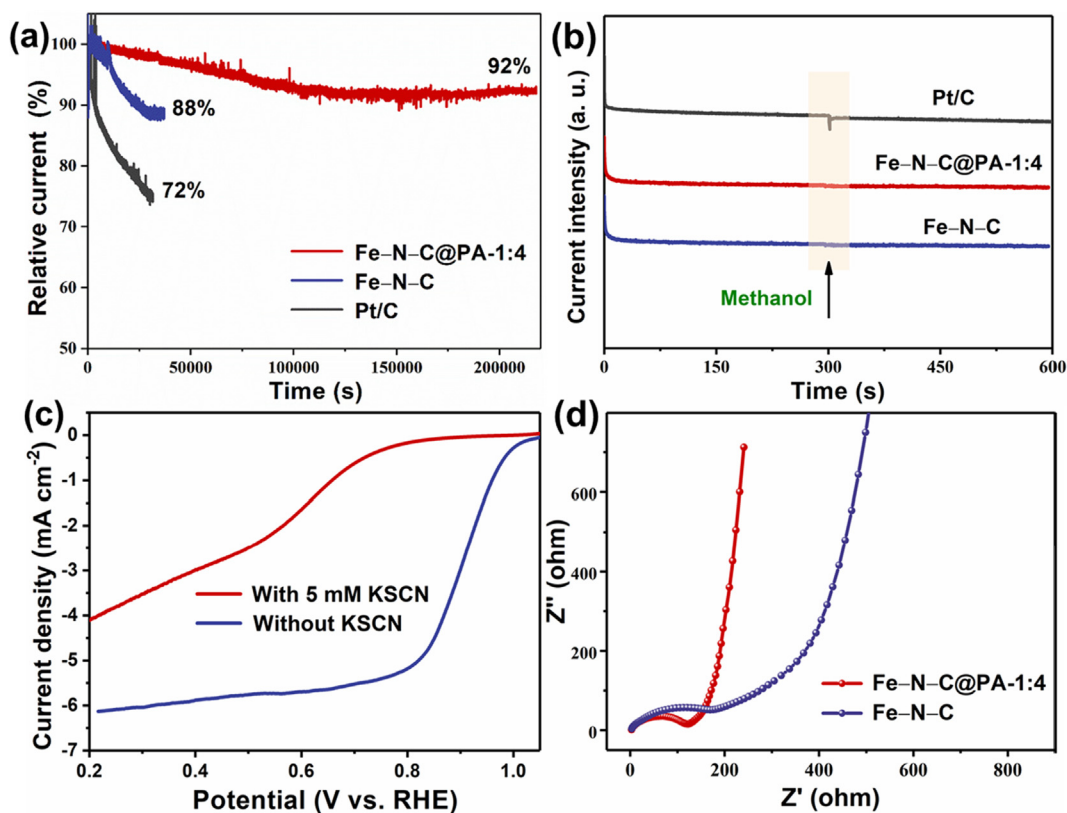
Q. Zhao, X. Tan, T. Ma et al.

Fig. 7. Chronoamperometry curves of Fe—N—C@PA-1:4, Fe—N—C and Pt/C (a). Methanol tolerance tests of Fe—N—C@PA-1:4, Fe—N—C and Pt/C (b). LSV curves of Fe—N—C@PA-1:4 with and without KSCN poisoning (c). EIS spectra of Fe—N—C and Fe—N—C@PA-1:4 (d).
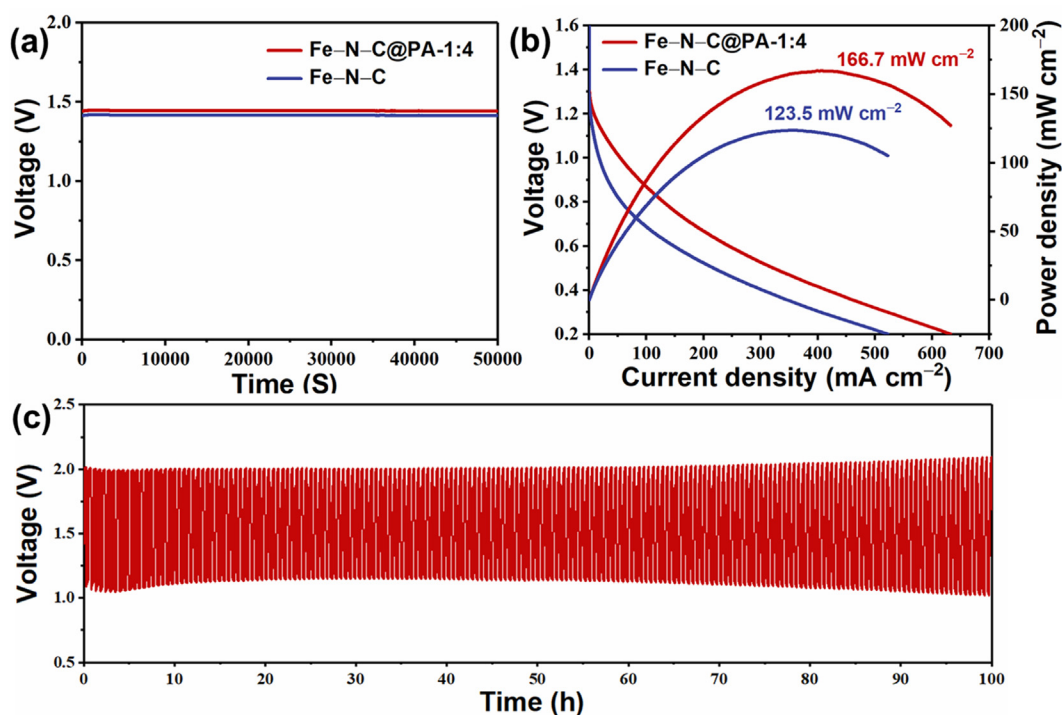

Fig. 8. Open-circuit voltage (a) and discharge polarization curves and power densities (b) of the zinc-air batteries based on Fe—N—C@PA-1:4 and Fe—N—C cathodes. Charge-discharge cycling curve of the Fe—N—C@PA-1:4-based zinc-air battery (c).

To sum up, atomically dispersed Fe—N—C@PA has been successfully fabricated through the layer-by-layer cladding template method. Fe(phen)$_x$ and MgO are considered to be the preferable metal precursor and template. With an optimized petroleum asphalt/template mass ratio of 1:4, the graphitic degree and conductivity of the carbon skeleton can be efficiently increased,

affording a conjugated electronic substrate to strengthen the atomic Fe—N$_x$ moieties. Owing to the fascinating porous structure with reinforced Fe—N$_x$ active sites, Fe—N—C@PA-1:4 provides almost a four-electron transfer pathway (3.96) and comparable electrocatalytic activity to the Fe—N—C counterpart with an E$_{1/2}$ of 0.90 V, outperforming the commercial Pt/C catalyst (E$_{1/2}$ = 0.86 V) in alkaline medium. Meanwhile, Fe—N—C@PA-1:4 exhibits superior durable stability and methanol tolerance to the Fe—N—C and Pt/C catalysts, delivering a high 92% current retention rate with prolonged 200,000 s. When employed as the air cathode in a zinc–air battery, the Fe—N—C@PA-1:4 catalyst delivers an outstanding power density of 166.7 mW cm^{-2}. Interestingly, the intercalation of petroleum asphalt achieves an impressive ~20% mass yield of the catalyst compared with Fe—N—C, providing a feasible avenue for the scalable synthesis of atomically dispersed catalysts towards ORR and the high value-added utilization of petroleum asphalt.

4. Conclusion

In summary, we have demonstrated a facile and cost-effective strategy for the scalable synthesis of atomically dispersed Fe—N—C derived from petroleum asphalt. Surface coating with appropriate amount of petroleum asphalt not only improve the graphitic degree and conductivity of the carbon skeleton to strengthen the atomic Fe—N$_x$ active species, but also significantly increases mass yield of the catalyst. The highly active and reinforced Fe—N$_x$ species endows Fe—N—C@PA-1:4 a robust electrocatalytic catalyst towards ORR. The Fe—N—C@PA-1:4 provides almost a four-electron transfer pathway and exhibits superior electrocatalytic activity to the commercial Pt/C catalyst, as well as reinforced durability and excellent methanol tolerance in alkaline medium. The Fe—N—C@PA-1:4 catalyst also presents remarkable performance when utilized as the cathode for a zinc-air battery. The results demonstrate the promising prospect for the scalable synthesis of cost-effective but efficient non-noble metal electrocatalysts for ORR and is waiting for practical applications in energy storage and conversion devices.

CRediT author statement

Qingshan Zhao: Investigation, Conceptualization, Writing - review & editing, Funding acquisition. **Xiaojie Tan:** Investigation, Data curation, Writing - original draft. **Tianwen Ma:** Investigation, Methodology, Writing - original draft. **Fengliang Cao:** Software, Methodology. Zhengzheng Xia: Investigation, Data curation. **Hui Liu:** Writing - original draft, Formal analysis. **Hui Ning:** Methodology, Validation. **Zhongtao Li:** Resources, Project administration. **Han Hu:** Resources, Project administration. **Mingbo Wu:** Writing - review & editing, Supervision, Funding acquisition.

Declaration of Competing Interest

The authors declare that they have no known competing financial interests or personal relationships that could have appeared to influence the work reported in this paper.

Acknowledgments

Appendix A. Supplementary material

Supplementary data to this article can be found online at https://doi.org/10.1016/j.jcis.2020.11.040.

References

[1] D. Lee, P. Xu, Z. Cano, A. Kashkooli, M. Park, Z. Chen, Recent progress and perspectives on bi-functional oxygen electrocatalysts for advanced rechargeable metal-air batteries, J. Mater. Chem. A 4 (2016) 7107–7134.

[2] D. Dekel, Review of cell performance in anion exchange membrane fuel cells, J. Power Sources 375 (2018) 158–169.

[3] M. Debe, Electrocatalyst approaches and challenges for automotive fuel cells, Nature 486 (2012) 43–51.

[4] N. Chaudhari, J. Joo, B. Kim, B. Ruqia, S. Choi, K. Lee, Recent advances in electrocatalysts toward the oxygen reduction reaction: the case of PtNi octahedra, Nanoscale 10 (2018) 20073–20088.

[5] M. Shao, Q. Chang, J. Dodelet, R. Chenitz, Recent advances in electrocatalysts for oxygen reduction reaction, Chem. Rev. 116 (2016) 3594–3657.

[6] G. Wu, P. Zelenay, Nanostructured nonprecious metal catalysts for oxygen reduction reaction, Acc. Chem. Res. 46 (2013) 1878–1889.

[7] F. Shao, X. Zhu, A. Wang, K. Fang, J. Yuan, J. Feng, One-pot synthesis of hollow AgPt alloyed nanocrystals with enhanced electrocatalytic activity for hydrogen evolution and oxygen reduction reactions, J. Colloid Interf. Sci. 505 (2017) 307–314.

[8] G. Chen, X. Yang, Z. Xie, F. Zhao, Z. Zhou, Q. Yuan, Hollow PtCu octahedral nanoalloys: efficient bifunctional electrocatalysts towards oxygen reduction reaction and methanol oxidation reaction by regulating near-surface composition, J. Colloid Interf. Sci. 562 (2020) 244–251.

[9] Y. Zhu, X. Chen, J. Liu, J. Zhang, D. Xu, W. Peng, Y. Li, G. Zhang, F. Zhang, X. Fan, Rational design of Fe/N/S-doped nanoporous carbon catalysts from covalent triazine frameworks for efficient oxygen reduction, Chemsuschem 11 (2018) 2402–2409.

[10] Y. Zhu, J. Sokolowski, X. Song, Y. He, Y. Mei, G. Wu, Engineering local coordination environments of atomically dispersed and heteroatom-coordinated single metal site electrocatalysts for clean energy-conversion, Adv. Energy Mater. 10 (2020) 1902844.

[11] Y. Peng, B. Lu, S. Chen, Carbon-supported single atom catalysts for electrochemical energy conversion and storage, Adv. Mater. 30 (2018) 1801995.

[12] X. Wei, X. Luo, H. Wang, W. Gu, W. Cai, Y. Lin, C. Zhu, Highly-defective Fe-N-C catalysts towards pH-universal oxygen reduction reaction, Appl. Catal. B-Environ. 263 (2020) 118347.

[13] Z. Chen, D. Zhao, C. Chen, Y. Xu, C. Sun, K. Zhao, M. Arif Khan, D. Ye, H. Zhao, J. Fang, X. Andy Sun, J. Zhang, Reconstruction of pH-universal atomic FeNC catalysts towards oxygen reduction reaction, J. Colloid Interf. Sci. 582 (2020) 1033–1040.

[14] N. Xue, J. Liu, P. Wang, C. Wang, S. Li, H. Zhu, J. Yin, Scalable synthesis of Fe$_3$N nanoparticles within N-doped carbon frameworks as efficient electrocatalysts for oxygen reduction reaction, J. Colloid Interf. Sci. 580 (2020) 460–469.

[15] C. Wang, W. Chen, K. Xia, N. Xie, H. Wang, Y. Zhang, Silk-derived 2D porous carbon nanosheets with atomically-dispersed Fe-N$_x$-C sites for highly efficient oxygen reduction catalysts, Small 15 (2019) 1804966.

[16] J. Han, X. Meng, L. Lu, J. Bian, Z. Li, C. Sun, Single-atom Fe-N$_x$-C as an efficient electrocatalyst for zinc-air batteries, Adv. Funct. Mater. 29 (2019) 1808872.

[17] Z. Miao, X. Wang, M. Tsai, Q. Jin, J. Liang, F. Ma, T. Wang, S. Zheng, B. Hwang, Y. Huang, S. Guo, Q. Li, Atomically sispersed Fe-N$_x$/C electrocatalyst boosts oxygen catalysis via a new metal-organic polymer supramolecule strategy, Adv. Energy Mater. 8 (2018) 1801226.

[18] X. Xu, Z. Xia, X. Zhang, R. Sun, X. Sun, H. Li, C. Wu, J. Wang, S. Wang, G. Sun, Atomically dispersed Fe-N-C derived from dual metal-organic frameworks as efficient oxygen reduction electrocatalysts in direct methanol fuel cells, Appl. Catal. B-Environ. 259 (2019) 118042.

[19] X. Zhang, X. Han, Z. Jiang, J. Xu, L. Chen, Y. Xue, A. Nie, Z. Xie, Q. Kuang, L. Zheng, Atomically dispersed hierarchically ordered porous Fe–N–C electrocatalyst for high performance electrocatalytic oxygen reduction in Zn-Air battery, Nano Energy 71 (2020) 104547.

[20] H. Hu, M. Wu, Heavy oil-derived carbon for energy storage applications, J. Mater. Chem. A 8 (2020) 7066–7082.

[21] H. Ning, Q. Zhao, H. Zhang, Z. Li, W. Wu, L. Wang, M. Wu, Application of petroleum asphalt-based carbon materials in electrochemical energy storage, Sci. China-Chem. 48 (2018) 329–341.

[22] X. Li, Q. Zhao, X. Feng, L. Pan, Z. Wu, X. Wu, T. Ma, J. Liu, Y. Pan, Y. Song, M. Wu, Pyridinic nitrogen-doped graphene nanoshells boost the catalytic efficiency of palladium nanoparticles for the N-allylation reaction, Chemsuschem 12 (2019) 858–865.

[23] T. Ma, X. Tan, Q. Zhao, Z. Wu, F. Cao, J. Liu, X. Wu, H. Liu, X. Wang, H. Ning, M. Wu, Template-oriented synthesis of Fe–N-codoped graphene Nnanoshells derived from petroleum pitch for efficient nitroaromatics reduction, Ind. Eng. Chem. Res. 59 (2020) 129–136.

Q. Zhao, X. Tan, T. Ma et al.

[24] L. Pan, Y. Wang, H. Hu, X. Li, J. Liu, L. Guan, W. Tian, X. Wang, Y. Li, M. Wu, 3D self-assembly synthesis of hierarchical porous carbon from petroleum asphalt for supercapacitors, Carbon 134 (2018) 345–353.

[25] J. Liu, Y. Liu, P. Li, L. Wang, H. Zhang, H. Liu, J. Liu, Y. Wang, W. Tian, X. Wang, Z. Li, M. Wu, Fe-N-doped porous carbon from petroleum asphalt for highly efficient oxygen reduction reaction, Carbon 126 (2018) 1–8.

[26] S. Hu, W. Ni, D. Yang, C. Ma, J. Zhang, J. Duan, Y. Gao, S. Zhang, Fe_3O_4 nanoparticles encapsulated in single-atom Fe-N-C towards efficient oxygen reduction reaction: Effect of the micro and macro pores, Carbon 162 (2020) 245–255.

[27] W. Liu, L. Zhang, X. Liu, X. Liu, X. Yang, S. Miao, W. Wang, A. Wang, T. Zhang, Discriminating catalytically active FeN_x species of atomically dispersed Fe-N-C catalyst for selective oxidation of the C-H bond, J. Am. Chem. Soc. 139 (2017) 10790–10798.

[28] Y. Fu, D. Xu, Y. Wang, X. Li, Z. Chen, K. Li, Z. Li, L. Zheng, X. Zuo, Single atoms anchored on cobalt-based catalysts derived from hydrogels containing phthalocyanine toward the oxygen reduction reaction, ACS Sustain. Chem. Eng. 8 (2020) 8338–8347.

[29] H. Liu, Q. Zhao, J. Liu, X. Ma, Y. Rao, X. Shao, Z. Li, W. Wu, H. Ning, M. Wu, Synergistically enhanced activity of nitrogen-doped carbon dots/graphene composites for oxygen reduction reaction, Appl. Surf. Sci. 423 (2017) 909–916.

[30] Q. Zhao, J. Liu, Y. Wang, W. Tian, J. Liu, J. Zang, H. Ning, C. Yang, M. Wu, Novel in-situ redox synthesis of Fe_3O_4/rGO composites with superior electrochemical performance for lithium-ion batteries, Electrochim. Acta 262 (2018) 233–240.

[31] Y. Chen, S. Ji, C. Chen, Q. Peng, D. Wang, Y. Li, Single-atom catalysts: Synthetic strategies and electrochemical applications, Joule 2 (2018) 1242–1264.

[32] J. Gu, C. Hsu, L. Bai, H. Chen, X. Hu, Atomically dispersed Fe^{3+} sites catalyze efficient CO_2 electroreduction to CO, Science 364 (2019) 1091–1094.

[33] Z. Zhang, J. Sun, F. Wang, L. Dai, Efficient oxygen reduction reaction (ORR) catalysts based on single iron atoms dispersed on a hierarchically structured porous carbon framework, Angew. Chem. Inter. Ed. 57 (2018) 9038–9043.

[34] C. Zhu, Q. Shi, B. Xu, S. Fu, G. Wan, C. Yang, S. Yao, J. Song, H. Zhou, D. Du, S. Beckman, D. Su, Y. Lin, Hierarchically porous M-N-C (M = Co and Fe) single-atom electrocatalysts with robust MN_x active moieties enable enhanced ORR performance, Adv. Energy Mater. 8 (2018) 1801956.

[35] J. Wu, M. Lin, X. Cong, H. Liu, P. Tan, Raman spectroscopy of graphene-based materials and its applications in related devices, Chem. Soc. Rev. 47 (2018) 1822–1873.

[36] J. Gautam, T. Thanh, K. Maiti, N. Kim, J. Lee, Highly efficient electrocatalyst of N-doped graphene-encapsulated cobalt-iron carbides towards oxygen reduction reaction, Carbon 137 (2018) 358–367.

[37] A. Kaniyoor, S. Ramaprabhu, A Raman spectroscopic investigation of graphite oxide derived graphene, AIP Adv. 2 (2012) 032183.

[38] J. Chen, W. Li, B. Xu, Nitrogen-rich Fe-N-C materials derived from polyacrylonitrile as highly active and durable catalysts for the oxygen reduction reaction in both acidic and alkaline electrolytes, J. Colloid Interf. Sci. 502 (2017) 44–51.

[39] C. Song, S. Wu, X. Shen, X. Miao, Z. Ji, A. Yuan, K. Xu, M. Liu, X. Xie, L. Kong, G. Zhu, S.A. Shah, Metal-organic framework derived Fe/Fe_3C@N-doped-carbon porous hierarchical polyhedrons as bifunctional electrocatalysts for hydrogen evolution and oxygen-reduction reactions, J. Colloid Interf. Sci. 524 (2018) 93–101.

[40] Y. Wang, X. Zhang, S. Xi, X. Xiang, Y. Du, P. Chen, D. Lyu, S. Wang, Z. Tian, P. Shen, Rational sesign and synthesis of hierarchical porous Mn-N-C nanoparticles with atomically dispersed MnN_x moieties for highly efficient oxygen reduction reaction, ACS Sustain. Chem. Eng. 8 (2020) 9367–9376.

[41] Z. Wu, S. Xu, Q. Yan, Z. Chen, Y. Ding, C. Li, H. Liang, S. Yu, Transition metal-assisted carbonization of small organic molecules toward functional carbon materials, Sci. Adv. 4 (2018) eaat0788.

[42] X. Wang, Y. Pan, H. Ning, H. Wang, D. Guo, W. Wang, Z. Yang, Q. Zhao, B. Zhang, L. Zheng, J. Zhang, M. Wu, Hierarchically micro- and meso-porous $Fe-N_4O$-doped carbon as robust electrocatalyst for CO_2 reduction, Appl. Catal. B-Environ. 266 (2020) 118630.

[43] C. Yang, L. Fu, R. Zhu, Z. Liu, Influence of cobalt species on the catalytic performance of $Co-N-C/SiO_2$ for ethylbenzene oxidation, Phys. Chem. Chem. Phys. 18 (2016) 4635–4642.

[44] Q. He, Y. Meng, H. Zhang, Y. Zhang, Q. Sun, T. Gan, H. Xiao, X. He, H. Ji, Amino-metalloporphyrin polymers derived Fe single atom catalysts for highly efficient oxygen reduction reaction, Sci. China Chem. 63 (2020) 810–817.

[45] R. Singh, R. Devivaraprasad, T. Kar, A. Chakraborty, M. Neergat, Electrochemical impedance spectroscopy of oxygen reduction reaction (ORR) in a rotating disk electrode configuration: effect of ionomer content and carbon-support, J. Electrochem. Soc. 162 (2015) 489–498.

[46] J. Luo, X. Qiao, J. Jin, X. Tian, H. Fan, D. Yu, W. Wang, S. Liao, N. Yu, Y. Deng, A strategy to unlock the potential of CrN as a highly active oxygen reduction reaction catalyst, J. Mater. Chem. A 8 (2020) 8575–8585.